School of Natural Sciences and Mathematics

Broadband Transient Absorption Study of Photoexcitations in Lead Halide Perovskites: Towards a Multiband Picture

Citation:

Anand, B., S. Sampat, E. O. Danilov, W. Peng, et al. 2016. "Broadband transient absorption study of photoexcitations in lead halide perovskites: Towards a multiband picture." Physical Review B - Condensed Matter and Materials Physics 93(16), doi:10.1103/PhysRevB.93.161205

PHYSICAL REVIEW B **93**, 161205(R) (2016)

Broadband transient absorption study of photoexcitations in lead halide perovskites: Towards a multiband picture

Benoy Anand,[1] Siddharth Sampat,[1] Evgeny O. Danilov,[2] Weina Peng,[3] Sara M. Rupich,[3] Yves J. Chabal,[3] Yuri N. Gartstein,[1] and Anton V. Malko[1,*]

[1]*Department of Physics, The University of Texas at Dallas, Richardson, Texas 75080, USA*

[2]*Department of Chemistry, North Carolina State University, Raleigh, North Carolina 27695, USA*

[3]*Department of Material Science and Engineering, The University of Texas at Dallas, Richardson, Texas 75080, USA*

(Received 29 January 2016; revised manuscript received 14 March 2016; published 22 April 2016)

Ultrafast transient pump-probe measurements of thin $CH_3NH_3PbI_3$ perovskite films over a wide spectral range from 350 to 800 nm reveal a family of photoinduced bleach (PB) and absorption (PA) features unequivocally pointing to the fundamentally multiband character of the underlying electronic structure. Excitation pump-energy dependent kinetics of three long-lived PB peaks at 1.65, 2.55, and 3.15 eV along with a broad PA band shows the involvement of band-edge thermalized carriers in all transitions and at least four, possibly more, electronic bands. The evolution of the transient signatures is described in terms of the redistribution of the conserved oscillator strength of the whole system. The multiband perspective opens up different directions for understanding and controlling photoexcitations in hybrid perovskites.

DOI: 10.1103/PhysRevB.93.161205

The meteoric rise of the power conversion efficiencies of perovskite solar cells [1–4] revolutionized the field of photovoltaics and also led to other promising applications of perovskites in light emitting diodes, tunable nanolasers, photodetectors, and thin film transistors [5–9]. These developments generated a tremendous experimental and theoretical research effort ranging from the fundamental questions of the photophysics of organic-inorganic hybrid perovskites [10] to various materials issues [4]. A comprehensive understanding of the fundamental photophysics would be conducive for a better utilization of perovskites in diverse optoelectronic applications.

Ultrafast pump-probe spectroscopy of semiconducting systems [11] is a powerful tool to explore the nature of optical excitations and their relaxation pathways. In the standard pump-probe setup, the excitation pulse is followed by monitoring the evolution of the spectral response of the system via the observation of the relative changes of the probe transmittance, $\Delta T/T$. These changes can exhibit both positive and negative values, usually referred to as photoinduced bleaching (PB) and absorption (PA), respectively. The assignment and interpretation of the PB and PA bands are essential parts of the analysis that can provide input for modeling the electronic structure and the system interactions.

Pump-probe spectroscopy has been actively used in studies on perovskites [12–14], including recent reports on the observation of the phonon bottleneck in the hot electron-hole relaxation process [15,16]. Most of the current literature concentrates on the quantitative analysis of PB and PA features in the spectral vicinity of the fundamental band gap, which is $\sim$1.65 eV for $CH_3NH_3PbI_3$ perovskites [12,13,15–17]. The model fitting is then based on the generic semiconductor picture with two parabolic bands and optical transitions between them and involves the notions of band state filling, band gap renormalization, and excitonic theory [18]. A broader look at the linear optical properties of perovskites (e.g., ellipsometric studies [19]) reveals, however, the presence of other absorption features suggesting the possible bearing of higher-energy electronic states on the pump-probe transients. In fact, another PB band was observed at $\sim$2.5 eV [12,13,20] and a short-lived PA feature at $\sim$0.8 eV discussed [14] in terms of the transitions between excitons originating from different electronic bands.

In this Rapid Communication, we report an observation of the third (PB3) long-lived PB band at $\sim$3.1–3.2 eV in $CH_3NH_3PbI_3$ perovskites (see Fig. 1). Along with PB features at $\sim$1.65 (PB1) and 2.5 eV (PB2), this clearly indicates that a comprehensive view of the photoinduced changes of the optical properties of perovskites requires a qualitatively broader, multiband description, beyond the picture [12,13] with one conduction and two valence bands. As we discuss below, such a multiband description would be consistent with the picture of the density functional theory (DFT)-derived electronic bands [21,22] in the vicinity of the R point of the Brillouin zone. The state-filling model suggests only a limited effect of photorefractive index changes on the spectra, advocating for the true excited state absorption contribution to the long-lived PA band between PB1 and PB2 features. Concomitant with a multiband model is the possibility of various *interband* transitions that might contribute to transients.

Polycrystalline $CH_3NH_3PbI_3$ perovskite films of $\sim$60 nm thickness and $\sim$1 μm average grain size [see Fig. S1 of the Supplemental Material (SM) [23]] are synthesized using the vapor assisted solution process (VASP) [24,25] and coated with a thin layer of poly(methyl methacrylate) (PMMA) to avoid degradation due to environmental moisture [26]. Time-resolved pump-probe measurements are based on an amplified Ti:sapphire laser system producing a fundamental beam with 100 fs pulses at 800 nm. For shorter wavelength measurements, the fundamental beam is frequency converted using an optical parametric amplifier to produce a 303 nm excitation pump, while part of the fundamental is used to generate a UV-stable white-light continuum (UV-WLC) probe in a CaF_2 crystal. Due

*anton.malko@utdallas.edu

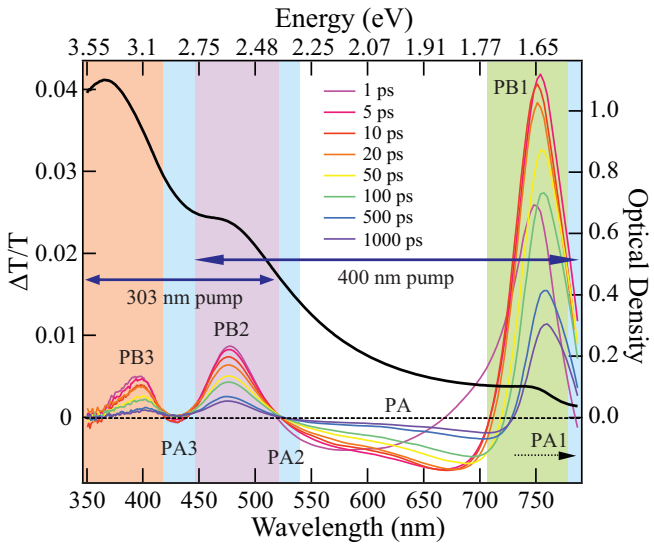

FIG. 1. Transient spectra measured in the 350–800 nm probe range for different time delays between pump and probe beams. Visible and near-UV parts of the spectrum here are taken with different excitation energies and matched to each other at the PB2 peak for $\geqslant$1 ps time delays to account for differences in photoexcitation levels. The colored bands are used to indicate the positions of various features: bleaches PB1 (green), PB2 (purple), PB3 (orange), and the broad long-lived PA (white) and the short-lived PA signals (blue) adjacent to PB bands. Also shown is the steady-state UV-vis linear absorption spectrum (black curve referring to the right axis).

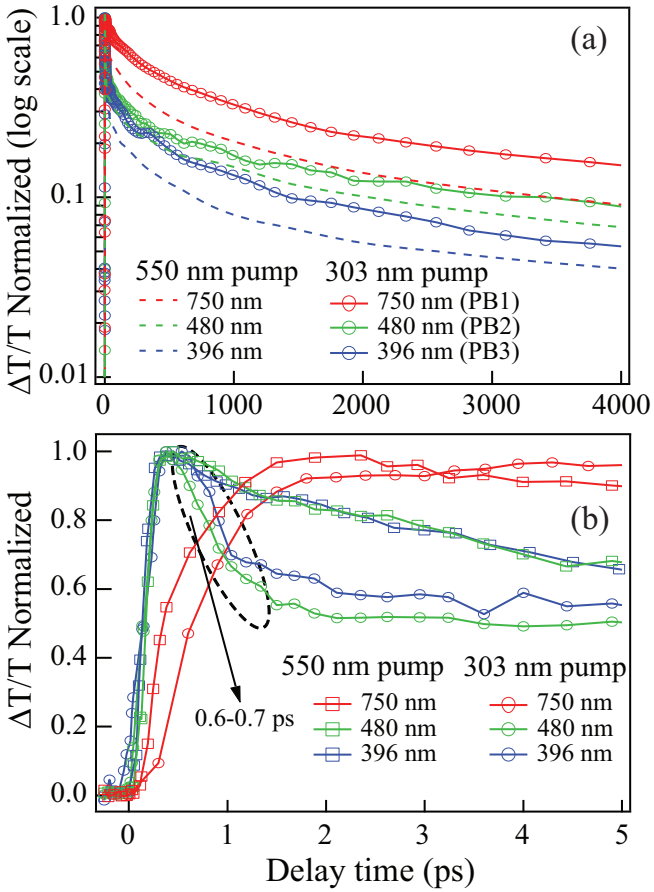

FIG. 2. Normalized kinetics at the PB peaks measured following excitation with different pumps (a) at longer time scales and (b) at shorter time scales. (a) clearly illustrates the similarity of the decay of all three PB peaks independently of the pump, in agreement with the band-edge depopulation of photoexcited carriers.

to UV-WLC fluctuations at longer wavelengths, optical filters are used to limit the detection window to the 350–520 nm range. For longer wavelength studies, a 400 nm pump is employed by doubling the fundamental beam, along with a visible WLC probe (450–800 nm) generated in a sapphire crystal. All measurements are made at room temperature.

Figure 1 displays the evolution of the broadband time-resolved differential transmission spectrum of the $CH_3NH_3PbI_3$ thin film derived with pumps at 303 and 400 nm. The spectrum prominently exhibits three well-defined PB features denoted as PB1 (~760 nm), PB2 (~480 nm), and PB3 (~390 nm). Importantly, the same three PB features are observed for the lower excitation energy pump at 550 nm (SM, Fig. S2). Figure 2 shows details of the kinetics of the PB bands for different pumps and at different time scales. It is evident that all three PB features are long lived and exhibit the same dynamics at long time scales independently of the pump. This suggests the similarity for their origin.

PB1 and PB2 bands have been previously observed using pump-probe and cw spectroscopy. They are commonly assigned [12,13] to the band-filling effects on the optical transitions between the two valence bands, VB1 and VB2, and the conduction band, denoted as CB1 in Fig. 3. These transitions are well matched with the absorption onsets in the steady-state absorption spectrum shown in Fig. 1 (black line). The PB3 feature we observe also agrees with the existence of another, higher-energy, band seen in the linear absorption spectrum as well as by ellipsometry [19]. We therefore assign the PB3 feature to band-filling-caused bleach of these higher-

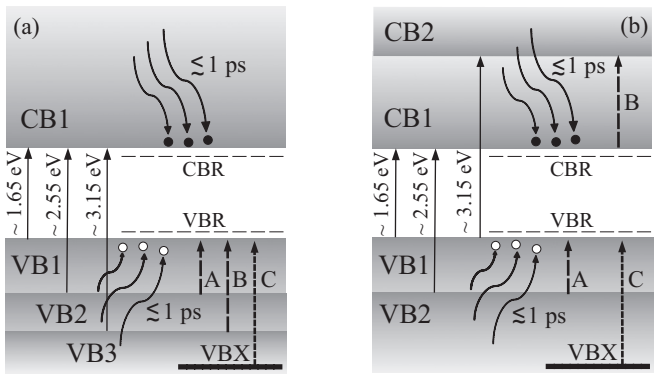

FIG. 3. Schematics of the alternative band diagrams: (a) The three valence bands (VB1, VB2, VB3) giving rise to optically allowed transitions into the conduction band (CB1) and (b) the two valence bands (VB1, VB2) giving rise to transitions into the two conduction bands (CB1, CB2). The common long-time dynamics of the three PB features reflects the population of the photoexcited carriers relaxed to the fundamental band edge(s). The displayed approximate transition energies correspond to the PB wavelengths monitored in Fig. 2. Also shown is the renormalization of the band edges (CBR and VBR) due to photoinduced changes in the exchange corrections to electronic energies [18]. See text for more discussion.

energy interband optical transitions. Our observations by themselves cannot uniquely specify the nature of the electronic bands involved: Figure 3 illustrates the two alternatives of the third valence band (VB3, transitions between VB3 and CB1) [Fig. 3(a)] or the second conduction band (CB2, transitions between VB1 and CB2) [Fig. 3(b)]. DFT calculations [21,22] indicate the presence of several bands in the vicinity of the R point of the Brillouin zone, and these alternatives are more consistent with computational results derived without or with spin orbit coupling (SOC), respectively.

The assignment involving the CB1 or VB1 band evidently agrees with the observed kinetics of the PB signatures. Indeed, Fig. 2(b) clearly shows a nearly identical rise of the PB2 and PB3 features following excitation by both higher-energy and lower-energy pumps. In the commonly discussed picture, hot carriers resulting from photoexcitation relatively quickly thermalize to the band edges of the CB1 and VB1 manifolds (SM, Fig. S3), and it is the population of these thermalized carriers that determines the quasiequilibrium behavior of the PB features already at picosecond time scales. The low excitation energy pump (550 nm, ∼2.25 eV) can only directly promote transitions between VB1 and CB1 bands, while our data show that all three PB signatures appear on a subpicosecond scale after photoexcitation, with their relative strength comparable to that of the higher-energy excitation conditions. This observation thus strongly indicates that one or both of the primary conduction and valence bands (CB1 and VB1) are involved in all three PB features, independently of pump energies.

In addition to the common longer-term kinetics, Fig. 2 also illustrates the differences of the shorter-term dynamics of the PB bands when excited by different pumps. Under 303 nm excitation, the early-time dynamics of PB2 and PB3 peaks shows a fast decay component (∼0.6–0.7 ps), while the PB1 dynamics exhibits the complementary rise. This behavior is similar to the previously observed [13] fast, ∼0.4 ps, initial decay of the PB2 peak after 400 nm pump excitation, which was attributed to the hot-hole relaxation from VB2 to VB1. Figure 2(b) shows that such a hot-hole-relaxation effect is absent for both PB2 and PB3 peaks when the pump energy is lowered to 2.25 eV. Some pump-dependent differences are also observed for the intermediate-term (∼50–500 ps) dynamics of the PB peaks in Fig. 2(a), due to various degrees of Auger-related carrier relaxation [27,28], with more data available in SM, Fig. S4. The subpicosecond decays observed for PB2 and PB3 early-time kinetics with a 303 nm pump would thus correspond to the hot carrier relaxation towards the fundamental band edge(s).

Pump-probe transients can be discussed in terms of spectral variations of the absorption coefficient $\Delta\alpha$ and the refraction index Δn or in terms of variations $\Delta\varepsilon$ of the complex dielectric function $\varepsilon = \varepsilon' + i\varepsilon''$ affected by photoexcitation of the system. These variations obey the Kramers-Kronig (KK) relations such as

$$\Delta n(\omega) = \frac{c}{\pi}\mathcal{P}\int_0^\infty \frac{\Delta\alpha(z)}{z^2-\omega^2}dz, \qquad (1)$$

where c is the speed of light [18,29]. Whether through KK considerations or quantum-mechanical sum rules [29,30], it is understood that the overall absorptive strength cannot change upon photoexcitation that conserves the total number of electrons in the system while causing only spectral redistribution:

$$\int_0^\infty \Delta\alpha(\omega)d\omega = 0, \quad \int_0^\infty \omega\Delta\varepsilon''(\omega)d\omega = 0. \qquad (2)$$

Since the excitation results in the production of free (or weaker bound) charge carriers, the sum rules (2) encompass both the low-frequency intraband transitions and various higher-frequency interband transitions. The contributions from the Drude-like conductivity of free electrons and holes in the parabolic CB and VB can be quantified by their effective plasma frequency $\omega_{\rm pl}$,

$$\int_0^{\omega_c} \omega\Delta\varepsilon''(\omega)d\omega = \frac{\pi\omega_{\rm pl}^2}{2}, \quad \omega_{\rm pl}^2 = \frac{n_{\rm eh}q^2}{\varepsilon_0 m_r}, \qquad (3)$$

where $n_{\rm eh}$ is the density of the photoexcited electrons (equal to that of holes), m_r the reduced electron-hole mass, and ω_c limits the integration to appropriate low frequencies. For the photoexcited carriers bound in excitons, the Drude conductivity should be replaced by the intraband absorption from the excitonic levels. As Eq. (3) is manifestly positive, the sum rules (2) must be compensated by the overall negative contribution from interband transitions (see SM, Fig. S5 for an illustration of this concept). Importantly, both $\Delta\alpha$ and Δn can cause variations of the sample transmittance ΔT. The need to include photorefractive changes in the analysis of transients in perovskites was recently advocated in Ref. [15], where the estimate of $m_r = 0.14m_e$ obtained this way is comparable to that derived from the magnetoabsorption [31]. We now stress that a "global fitting" [15] of ΔT must self-consistently [Eq. (1)] include multiple PB and PA features encountered over a broad spectral range, rather than just those near the fundamental band gap.

Figure 4 shows the dynamics and spectral evolution of various PA features in the broad visible region. One source for the transient photoinduced absorption ($\Delta T < 0$, $\Delta\alpha > 0$) commonly discussed in the perovskite literature [15,16] is band gap renormalization (BGR), a phenomenon that is known for semiconductors [11,18]. The schematics in Fig. 3 illustrates how BGR would result from the renormalization of the conduction (CBR) and valence (VBR) bands, which is caused by variation of the Coulomb exchange corrections due to the presence of photoexcited carriers [18]. As BGR has been used to readily explain the appearance of the short-lived ($\lesssim$1 ps) PA1 slightly below the energy of the PB1 peak [at 785 nm, Figs. 1 and 4(b)], similar appearances are expected below the PB2 and PB3 peaks in our multiband scheme. This is in fact what we observed (PA2 and PA3 bands shown in light blue in Fig. 1), and the similarity of the short-time decay of the PA features adjacent to PB1 and PB3 peaks is evidenced in the inset of Fig. 4(a).

A major evolution of the PA signal shown in Fig. 4(b) is seen in the 520–700 nm range. Initially this band exhibits a short-time (first several ps) redshift, similar to the spectral shift of the PB1 peak, which was assigned to the dynamic Burstein-Moss (BM) effect, indicating the carriers' thermalization [12]. At intermediate-time ranges (∼50–200 ps) the PA signal exhibits a spectrally dependent decay due to Auger facilitated relaxation [27,28]. Finally, at times $\gtrsim$1 ns, the decay converges

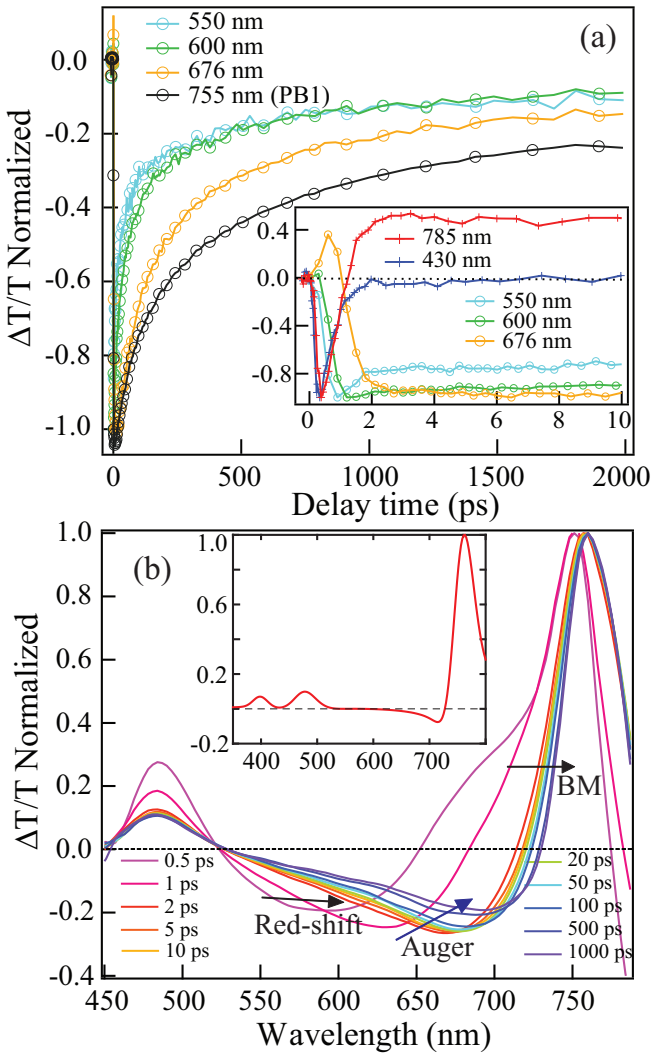

FIG. 4. (a) Dynamics of the visible PA measured at different spectral positions. For a visual comparison, the PB1 dynamics (sign reversed) is also shown. The inset showing the early-time dynamics reveals a similar short-lived nature of PA near PB1 and PB3 peaks. (b) Normalized transient spectra obtained with the 400 nm pump for the initial $n_{eh} \sim 1.7 \times 10^{18}$ cm^{-3} displaying the behavior of the broad PA band between PB1 and PB2 features. The arrows indicate the directions of the evolution of the spectrum. The inset illustrates computational results that would follow from the state-filling model with an account of the photorefractive index change Δn.

to a spectrally uniform pattern, whose similarity with the decay of the PB1 peak is evident in Fig. 4(a). This similarity at longer times suggests that the broad PA and PB1 features are related to the same thermalized species near the band edge(s).

One could try to explain the equilibrated behavior of this PA between the PB1 and PB2 peaks as a photorefractive effect [15] since, indeed, Δn can lead to negative ΔT appearing thus as PA higher than the energy of the PB1 feature. We computed the corresponding changes in the samples' transmittance that would follow from the state-filling model using the experimentally derived [19] dielectric function $\varepsilon(\omega)$ (see SM and Fig. S6 for details of the model). The illustration of the results in the inset of Fig. 4(b) clearly shows that this effect by itself is not sufficient: The relative magnitude and the spectral width of the PA experimentally observed at long times are substantially larger than the computed values, hence, the true $\Delta\alpha$-related absorption need to be in place involving the equilibrated photoexcited carriers.

The multiband pictures of Fig. 3 indicate that various *interband* transitions might contribute to positive $\Delta\alpha$ in the transients, such as the near-IR transitions denoted "A" and "B" in the figure. Since, however, the transitions defining the linear absorption are definitely electric-dipole allowed, the "A" and "B" transitions are expected to be electric-dipole forbidden [21,29,30]. A PA feature at 0.8 eV that could correspond to the "A" transition was reported [14], but it was short lived. This feature was actually attributed in Ref. [14] to the transition between the allowed and forbidden excitons, and an alternative explanation may be that the optical selection rule is effectively lifted during the process of the hot electron-hole relaxation. We note that DFT calculations [21,22] show the presence of several valence bands in the vicinity of the R point; it may then be possible that some of those bands would lead to the optically allowed PA, as exemplified in the sketch of Fig. 3 by the hypothetical valence band VBX. Assuming that the transition from VBX to CB1 is forbidden, and therefore not manifested in the linear absorption, transition "C" from VBX to VB1 would be allowed to contribute to the broad PA feature observed between the PB1 and PB2 peaks. The kinetics of this feature could also be affected by the dynamic redistribution of the oscillator strengths due to the state-filling and Coulomb effects.

Our experimental findings in this Rapid Communication reveal a rich structure of PB and PA features and unequivocally point to the fundamentally multiband character of the broad-band pump-probe transients in hybrid perovskites, providing thus an important input for understanding their electronic structure beyond traditional simplifying assumptions [18] of the parabolic bands and Elliott's excitonic absorption. A precise refinement of the multiband picture, including the role of SOC, should become possible with further experimental (such as near-IR pump-probe and charge injection) and computational studies.

We thank A. R. S. Kandada (Instituto Italiano di Technologia) for valuable discussions. This work was supported by the US Department of Energy Office of Science BES Award No. DE-SC0010697.

[1] M. Grätzel, Nat. Mater. **13**, 838 (2014).
[2] M. A. Green, A. Ho-Baillie, and H. J. Snaith, Nat. Photonics **8**, 506 (2014).
[3] M. D. McGehee, Nat. Mater. **13**, 845 (2014).
[4] M. A. Green and T. Bein, Nat. Mater. **14**, 559 (2015).
[5] S. D. Stranks and H. J. Snaith, Nat. Nanotechnol. **10**, 391 (2015).
[6] Z. K. Tan, R. S. Moghaddam, M. L. Lai, P. Docampo, R. Higler, F. Deschler, M. Price, A. Sadhanala, L. M. Pazos, D.

Credgington, F. Hanusch, T. Bein, H. J. Snaith, and R. H. Friend, Nat. Nanotechnol. **9**, 687 (2014).

[7] H. Zhu, Y. Fu, F. Meng, X. Wu, Z. Gong, Q. Ding, M. V. Gustafsson, M. T. Trinh, S. Jin, and X. Y. Zhu, Nat. Mater. **14**, 636 (2015).

[8] L. Dou, Y. Yang, J. You, Z. Hong, W. H. Chang, G. Li, and Y. Yang, Nat. Commun. **5**, 5404 (2014).

[9] X. Y. Chin, D. Cortecchia, J. Yin, A. Bruno, and C. Soci, Nat. Commun. **6**, 7383 (2015).

[10] Y. Hsiao, T. Wu, M. Li, Q. Liu, W. Qin, and B. Hu, J. Mater. Chem. A **3**, 15372 (2015).

[11] J. Shah, *Ultrafast Spectroscopy of Semiconductors and Semiconductor Nanostructures* (Springer, Heidelberg, 1999).

[12] J. S. Manser and P. V. Kamat, Nat. Photonics **8**, 737 (2014).

[13] G. C. Xing, N. Mathews, S. Y. Sun, S. S. Lim, Y. M. Lam, M. Grätzel, S. Mhaisalkar, and T. C. Sum, Science **342**, 344 (2013).

[14] C. X. Sheng, C. Zhang, Y. Zhai, K. Mielczarek, W. Wang, W. Ma, A. Zakhidov, and Z. V. Vardeny, Phys. Rev. Lett. **114**, 116601 (2015).

[15] M. B. Price, J. Butkus, T. C. Jellicoe, A. Sadhanala, A. Briane, J. E. Halpert, K. Broch, J. M. Hodgkiss, R. H. Friend, and F. Deschler, Nat. Commun. **6**, 8420 (2015).

[16] Y. Yang, D. P. Ostrowski, R. M. France, K. Zhu, J. V. D. Lagemaat, J. M. Luther, and M. C. Beard, Nat. Photonics **10**, 53 (2016).

[17] G. Grancini, A. R. S. Kandada, J. M. Frost, A. J. Barker, M. D. Bastiani, M. Gandini, S. Marras, G. Lanzani, A. Walsh, and A. Petrozza, Nat. Photonics **9**, 695 (2015).

[18] H. Haug and S. W. Koch, *Quantum Theory of the Optical and Electronic Properties of Semiconductors* (World Scientific, Singapore, 2004).

[19] P. Löper, M. Stuckelberger, B. Niesen, J. Werner, M. Filipič, S. J. Moon, J. H. Yum, M. Topič, S. De Wolf, and C. Ballif, J. Phys. Chem. Lett. **6**, 66 (2015).

[20] K. G. Stamplecoskie, J. S. Manser, and P. V. Kamat, Energy Environ. Sci. **8**, 208 (2014).

[21] J. Even, L. Pedesseau, and C. Katan, J. Phys. Chem. C **118**, 11566 (2014).

[22] G. Giorgi, J. I. Fujisawa, H. Segawa, and K. Yamashita, J. Phys. Chem. C **118**, 12176 (2014).

[23] See Supplemental Material at http://link.aps.org/supplemental/10.1103/PhysRevB.93.161205 for details of the sample structure, additional pump-probe data and computational details of transient transmittance based on the state filling model.

[24] Q. Chen, H. P. Zhou, Z. R. Hong, S. Luo, H. S. Duan, H. H. Wang, Y. S. Liu, G. Li, and Y. Yang, J. Am. Chem. Soc. **136**, 622 (2014).

[25] W. Peng, B. Anand, L. Liu, S. Sampat, B. E. Bearden, A. V. Malko, and Y. J. Chabal, Nanoscale **8**, 1627 (2016).

[26] J. A. Christians, P. A. M. Herrera, and P. V. Kamat, J. Am. Chem. Soc. **137**, 1530 (2015).

[27] G. Xing, N. Mathews, S. S. Lim, N. Yantara, X. Liu, D. Sabba, M. Grätzel, S. Mhaisalkar, and T. C. Sum, Nat. Mater. **13**, 476 (2014).

[28] O. Flender, J. R. Klein, T. Lenzer, and K. Oum, Phys. Chem. Chem. Phys. **17**, 19238 (2015).

[29] M. Dressel and G. Grüner, *Electrodynamics of Solids* (Cambridge University Press, Cambridge, U.K., 2002).

[30] Y. Toyozawa, *Optical Processes in Solids* (Cambridge University Press, Cambridge, U.K., 2003).

[31] A. Miyata, A. Mitioglu, P. Plochocka, O. Portugall, J. T. W. Wang, S. D. Stranks, H. J. Snaith, and R. J. Nicholas, Nat. Phys. **11**, 582 (2015).